TU Delft

Delft University of Technology

Assessing the Effectiveness of the IJmuiden Salt Screen Design for Nonuniform Selective Withdrawal by Physical and Numerical Modeling

De Fockert, Anton; O'Mahoney, Tom S.D.; Nogueira, Helena I.S.; Oldenziel, Gosse; Bijlsma, Arnout C.; Janssen, Hans

DOI
10.1061/(ASCE)HY.1943-7900.0001958

Publication date
2022

Document Version
Final published version

Published in
Journal of Hydraulic Engineering

Citation (APA)
De Fockert, A., O'Mahoney, T. S. D., Nogueira, H. I. S., Oldenziel, G., Bijlsma, A. C., & Janssen, H. (2022). Assessing the Effectiveness of the IJmuiden Salt Screen Design for Nonuniform Selective Withdrawal by Physical and Numerical Modeling. *Journal of Hydraulic Engineering*, *148*(2), Article 05021011. https://doi.org/10.1061/(ASCE)HY.1943-7900.0001958

Important note
To cite this publication, please use the final published version (if applicable).
Please check the document version above.

Copyright
Other than for strictly personal use, it is not permitted to download, forward or distribute the text or part of it, without the consent of the author(s) and/or copyright holder(s), unless the work is under an open content license such as Creative Commons.

Takedown policy
Please contact us and provide details if you believe this document breaches copyrights.
We will remove access to the work immediately and investigate your claim.

This work is downloaded from Delft University of Technology.
For technical reasons the number of authors shown on this cover page is limited to a maximum of 10.

Green Open Access added to TU Delft Institutional Repository

'You share, we take care!' - Taverne project

https://www.openaccess.nl/en/you-share-we-take-care

Otherwise as indicated in the copyright section: the publisher is the copyright holder of this work and the author uses the Dutch legislation to make this work public.

Case Study

Assessing the Effectiveness of the IJmuiden Salt Screen Design for Nonuniform Selective Withdrawal by Physical and Numerical Modeling

Anton de Fockert[1]; Tom S. D. O'Mahoney[2]; Helena I. S. Nogueira[3]; Gosse Oldenziel[4]; Arnout C. Bijlsma[5]; and Hans Janssen[6]

Abstract: Salt water intrusion through the New Sea Lock of IJmuiden, Netherlands requires mitigation to ensure availability of enough fresh water further inland. For this purpose, a salt screen has been proposed for selective withdrawal of salt water from the Noordzeekanaal in the vicinity of the lock complex. Formulas to assess the withdrawal rate of selective withdrawal are based on idealized layouts and conditions. In the case of IJmuiden, the flow surrounding a salt screen has a strong nonuniform character, such that these formulas are not applicable to predict the correct withdrawal rate and the effectiveness of selective withdrawal accurately. In this case physical scale modeling or computational fluid dynamics (CFD) modeling can be applied. This article discusses the limitations of the formulas for a three-dimensional (3D) flow application near the locks of IJmuiden and presents the use of CFD and physical scale model research to assess the flow patterns around the salt screen and the effectiveness of selective withdrawal. The CFD model was validated against the physical scale model and represented the complex flow fields around the salt screen to within acceptable deviations for both steady and transient states. This gives confidence in applying these more advanced modeling tools for the design and positioning of salt screens in confined complex 3D flow areas.
DOI: 10.1061/(ASCE)HY.1943-7900.0001958. *© 2021 American Society of Civil Engineers.*

Author keywords: Selective withdrawal; Salt screen; Salt intrusion; New sea lock IJmuiden; CFD validation; Physical scale model; Particle image velocimetry (PIV); Three-dimensional particle tracking velocimetry (3D-PTV); Density measurements; Density currents.

Introduction

The lock complex at IJmuiden (Fig. 1) in the Netherlands is the point of entrance for seagoing vessels into the Noordzeekanaal, leading to the port of Amsterdam. The Noordzeekanaal is connected to water bodies that are used as a source of fresh water for industry, agriculture, and for drinking water. Operating the locks for shipping traffic leads to salt water entering the canal (Kerstma et al. 1994). Owing to the construction of a new larger shipping lock (Nogueira et al. 2018), the salt intrusion through the lock complex is expected to increase if no mitigation measures are taken (locks labeled new and old, respectively, in Fig. 1). Because of the large depth of the Noordzeekanaal, the salt water from the locks will penetrate far inland, up to the connecting Amsterdam-Rijnkanaal. In addition, fresh water availability is at risk due to climate change with sea level rise and the increased frequency and intensity of droughts (van den Brink et al. 2019). For the Noordzeekanaal, the historical measure for mitigation of salt intrusion has been flushing the canal into the North Sea via the pumping station and discharge sluices north of the lock complex. However, in the dry year of 2018, not enough water was available for this measure and additional (temporary) measures were needed to keep the salt concentration in the canal within acceptable levels. The environmental impact assessment of the new lock was based on the requirement that the operation of the new sea lock does not lead to an increase in salt concentration further inland. In order to achieve this, additional (permanent) mitigation measures are required. There are a number of mitigation measures possible at sea locks (Abraham and van der Burgh 1964; Van der Kuur 1986; Kerstma et al. 1994). The method of selective withdrawal will be applied in the case of IJmuiden by placing a salt screen in the existing channel to the discharge sluices and pumping station. A similar system has been employed since 1973 in the north of the Netherlands, at the pumping station De Helsdeur near a smaller sea lock near Den Helder (Kerstma et al. 1994). Owing to the requirements of the government and other stakeholders of the canal, the salt screen at IJmuiden needs to be designed for a range of discharges through the sluices and pumps up to about 300 m^3/s (extreme discharges may reach up to 960 m^3/s).

Because the inlet channel to the pumping station and discharge sluices in the Binnenspuikanaal is shallower than the Noordzeekanaal, the salt water from the locks will accumulate in the Noordzeekanaal due to gravity. By installing a salt screen with an opening of 560 m^2 (80 m wide and 7 m deep) at the entrance of the Binnenspuikanaal (Fig. 2), selective withdrawal is facilitated to discharge

[1]Senior Researcher—Advisor, Hydraulic Engineering, Dept. of Hydraulics for Industry and Infrastructure, Deltares, 2629 HV Delft, Netherlands (corresponding author). Email: anton.defockert@deltares.nl

[2]Senior Researcher—Advisor, Hydraulic Engineering, Dept. of Hydraulics for Industry and Infrastructure, Deltares, 2629 HV Delft, Netherlands.

[3]Researcher—Advisor, Hydraulic Engineering, Dept. of Hydraulics for Industry and Infrastructure, Deltares, 2629 HV Delft, Netherlands.

[4]Researcher—Advisor, Hydraulic Engineering, Dept. of Hydraulics for Industry and Infrastructure, Deltares, 2629 HV Delft, Netherlands; Researcher, Laboratory for Aero- and Hydrodynamics, Faculty of 3mE, Delft Univ. of Technology, 2628 CA Delft, Netherlands.

[5]Senior Researcher—Advisor, Hydraulic Engineering, Dept. of Harbour, Coastal and Offshore Engineering, Deltares, 2629 HV, Delft, Netherlands.

[6]Senior Advisor, Dept. of Major Projects and Maintenance, Rijkswaterstaat, P.O. Box 24057, 3502 MB Utrecht, Netherlands.

Note. This manuscript was submitted on October 30, 2020; approved on September 13, 2021; published online on December 15, 2021. Discussion period open until May 15, 2022; separate discussions must be submitted for individual papers. This paper is part of the ***Journal of Hydraulic Engineering***, © ASCE, ISSN 0733-9429.

Downloaded from ascelibrary.org by Technische Universiteit Delft on 01/09/23. Copyright ASCE. For personal use only; all rights reserved.

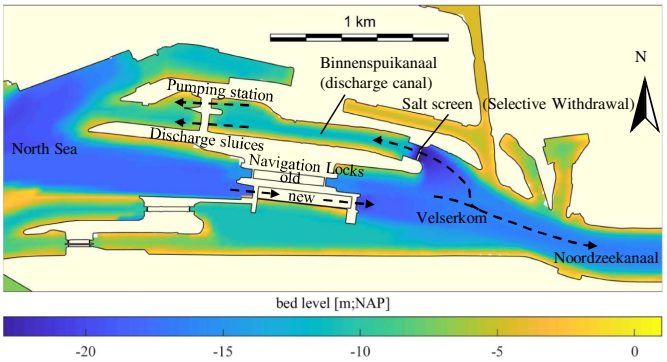

Fig. 1. Map of the IJmuiden Locks and Discharge Complex with the location of the salt screen. The salt water from the North Sea enters the Velserkom through the locks. By means of selective withdrawal, the additional salt in the Velserkom will be discharged back to the North Sea through the discharge canal, sluices, and pumping station north of the locks. The dashed lines show the transit of the saltwater.

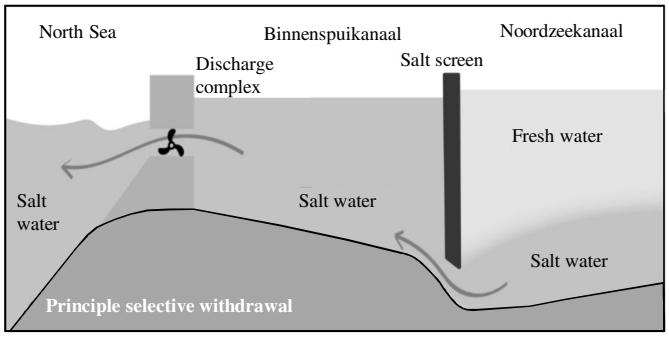

Fig. 2. Schematic representation of the salt screen at the entrance of the Binnenspuikanaal, allowing mainly salt water to flow to the discharge sluices and pumping station. (Reprinted with permission from Rijkswaterstaat.)

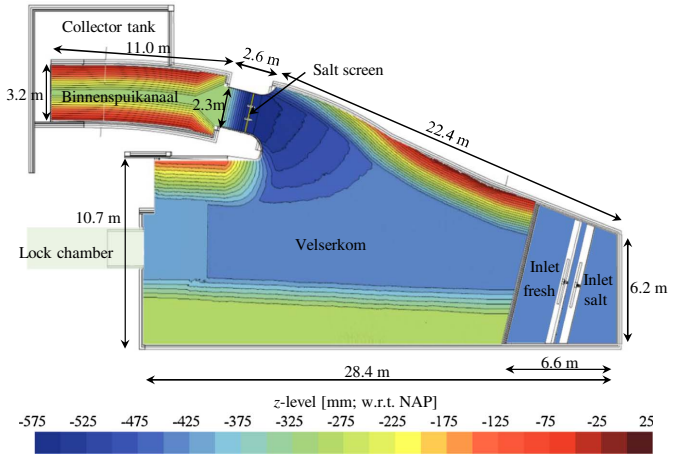

Fig. 3. Overview of the physical scale model with main dimensions including bathymetry in model scale (relative to Amsterdam Ordnance Datum–NAP on model scale).

mainly salt water from the deeper parts of the Velserkom to the sluices and the pumping station and eventually to the North Sea. Installing a salt screen at this location in an already existing structure, surrounded by other infrastructure, does not allow for a hydrodynamically optimal design for fully effective selective withdrawal.

Selective withdrawal can be an effective measure to subtract water from a specific layer of a stratified water body. Selective withdrawal has seen many applications in the management of water quality in reservoirs (see e.g., Imberger 1980; Thendrup 1980), for cooling water intake at thermal power stations (e.g., Harleman and Elder 1965; Ettema et al. 2005), and for shipping locks (Mausshardt and Singelton 1995). Selective withdrawal is used here to describe the process in stratified reservoirs whereby the discharge through an outlet of the reservoir is made wholly or primarily from a single stratified layer. As the stratification significantly reduces momentum exchange in the vertical direction, a horizontal flow can be initiated at a certain level to extract water from that level.

Theoretical work on the physical processes that are relied upon in selective withdrawal has focused on two-dimensional (2D) flows of two-layer fluids (e.g., Hocking 1991, 1995). The three-dimensional (3D) characteristics of the flow are neglected in most cases because the effects are usually limited to a smooth contraction of the flow from the reservoir into an outlet channel with a horizontal bed (e.g., Harleman and Elder 1965; Wood and Lai 1972; Delft Hydraulics Laboratory 1973; Jirka 1979; Yu et al. 2004) such that the flow upstream and downstream of the outlet in the channel is still uniform across the width. This represents a line sink. Some studies are available for point sinks with a uniform approach flow channel (e.g., Jirka and Katavola 1979) and for outlets (both two- and three-dimensional) in a linearly stratified reservoir (e.g., Wood 2001). A review of these and other similar studies is given in Fan (2008). The emphasis of most of these studies has been in finding the limiting withdrawal ratio for which the lower layer is withdrawn without the upper layer being withdrawn.

The line sink outlet is created in practice by a skimmer wall or salt screen. Harleman and Elder (1965) investigated different types of skimmer walls to subtract the cold water from a reservoir. They performed physical model tests using salt and fresh water and found that the densimetric Froude number and the level of the interface determine whether a skimmer wall will lead to effective selective withdrawal. Jirka (1979) expanded on the data set generated by Harleman and Elder and updated the effectiveness diagram with the rate of effectiveness of a skimmer wall by using the measurement data of Delft Hydraulics Laboratory (1973). He also found the incipient withdrawal flow to be independent of the skimmer wall conditions when the opening under the skimmer wall is lower than 2/3 of the height of the interface. Shamaa and Zhu (2010) performed an experimental study on the use of a curtain to control the temperature from a two-layer stratified reservoir. In this analysis, the flow is measured by means of particle image velocimetry (PIV) and laser induced fluorescence (LIF) in a flume presenting the detailed description of the flow around the curtain.

The above reported studies of selective withdrawal have been performed for small two-dimensional applications, where the interface is constant over the width of the selective withdrawal. For a salt screen with a uniform approach channel in width, the diagrams by Jirka (1979) could be used to assess the behavior of the selective withdrawal. Relatively small 3D effects in the close vicinity to the point of extraction (such as shape of the intake structure) have been accounted for in the past (Fan 2008). However, for the IJmuiden location, the cross-sectional area of the entire inflow channel decreases abruptly by a factor of 3 between the entrance to the Binnenspuikanaal and the opening at the salt screen (Fig. 3). As the level of the interface between layers and the mixing between layers is dependent on the velocity difference between the layers, the empirical formulas

Downloaded from ascelibrary.org by Technische Universiteit Delft on 01/09/23. Copyright ASCE. For personal use only; all rights reserved.

that assume a uniform flow velocity in the width upstream of the screen will incorrectly characterize this flow. If the width at the screen is used, the velocities will be too high in the approach channel. Similarly, due to the expected oblique flow at the entrance of the Binnenspuikanaal near the approach harbors of the navigation locks (Fig. 1), complex three-dimensional flow patterns including flow detachment and buoyancy effects will be present. In combination with the bottom geometry near the salt screen (Fig. 2) and the gradual interface between salt and fresh water, all these aspects will lead to significant discrepancies between the empirical relations available in literature and the achieved withdrawal ratio.

The effect of all of these aspects on the withdrawal ratio could be studied by means of physical modeling, as has been done in the past for the salt screen in Den Helder (Kerstma et al. 1994). Numerical investigations have almost all been limited to the simplest of outtake and channel geometries and compared with theory or experiments in those cases (Farrow and Hocking 2006; Boschetti et al. 2017; Islam et al. 2018). Due to the lack of validation cases in literature on three-dimensional effects near a selective withdrawal, validation is needed to assess whether a computational fluid dynamics (CFD) model can be used to correctly represent three-dimensional flow patterns near the salt screen. In this article, the withdrawal ratio of the proposed salt screen for selective withdrawal at IJmuiden is studied with physical scale modeling and by a CFD model validated against the physical scale model tests.

Materials and Methods

Physical Model

Physical scale model tests were performed in the Deltares Lock Facility at a scale of 1:40. The scale model covered the inner approach harbor (Velserkom), the salt screen and part of the Binnenspuikanaal (Fig. 3). The salt screen in the physical model is supported by two pillars and consists of three openings 17.5 cm high, with a width of 68.5 cm (outer openings) and 62.5 cm (center opening). The bottom edge of the salt screen is curved to limit flow contraction. The salt screen has open chambers at the back providing space for the recirculation current generated at the tip. The flow direction toward the salt screen is mainly from the Velserkom and the Noordzeekanaal. In IJmuiden, the salt water enters the Velserkom via the lock, after which it is transported further inland by density currents. The salt water in the Velserkom collects near the bed in the periods between the flushing windows at low tide. This was represented in the boundary conditions of the physical scale model tests, where the inlet boundary condition is located in the Velserkom near the entry of the Noordzeekanaal (Figs. 3 and 4). Salt intrusion directly from the lock chamber to the salt screen and discharge channel was not considered in the validation tests but has been studied numerically.

The model was scaled keeping the Froude number ($\mathrm{Fr} = U\sqrt{gh}$) and the densimetric Froude number ($\mathrm{Fr}_{\mathrm{dens}=} U_s\sqrt{g'h_s}$, with $g' = g\Delta\rho/\rho$) equal in model and prototype, where U is the flow velocity, U_s is the velocity of the salt layer, g is the gravitational acceleration, h is the water depth, h_s is the depth of the salt layer, and ρ is the density. The relatively large geometrical scale of 1:40 was chosen to ensure that the turbulent mixing represented by the Richardson number (θ) was able to create sufficient mixing in the model. Monish (1938) reformulated the Richardson number to be easily applicable in experiments. Monish (1938) proposed to use the reciprocal of the Richardson number, which is a ratio between the gravitational force multiplied by the viscous force and the inertial force, defined as

$$\frac{1}{\vartheta'} = \frac{\rho}{\Delta\rho}\frac{u_{\mathrm{rel}}^3}{g\nu} \tag{1}$$

where u_{rel} = relative flow velocity between the salt and fresh layer; and ν = kinematic viscosity. To avoid significant scale effects, the reciprocal of the Monish number (ϑ') should be larger than 175 (Delft Hydraulics Laboratory 1958), which is the case for velocities larger than 3 cm/s in the physical model.

The salt water (density 1,014.9 kg/m^3) and fresh water (density 998.8 kg/m^3) entered the model by flowing over the edges of two separate rectangular boxes at the inlet section. Between the two boxes, a separation plate was installed to prevent early mixing. The fresh water inflow was at the side of the scale model (Fig. 3) and the salt water flowed under the separation plate into the model. This created the desired two-layered flow. Two meters downstream of the inlet, the water flowed through flow stabilization pipes to ensure a uniform flow in the model toward the salt screen. Downstream of the salt screen, the flow entered the Binnenspuikanaal where it was discharged over an adjustable linear free overflow weir. The mixed water from the model flowed into the collector tank from where it was pumped to a mixing tank. In the mixing tank the water was upgraded to the required density for reuse at the inflow boundary. The remainder of the water was discharged.

The set of boundary conditions applied in the physical model cannot be used to directly assess the effectiveness of the salt screen since a fixed salt flux is prescribed at the inlet of the physical model, which is automatically present at the outlet. At the salt screen in the Binnenspuikanaal (Fig. 2), the salt flux is determined by the salinity profile at the Velserkom (inlet) and the discharge at the discharge sluices and pumping station (outlet). Alternative boundary conditions were tested (a discharge boundary at the outlet with a density profile at the inlet) but it turned out that this combination of boundary conditions did not lead to a representative flow behavior around the salt screen due to the strong stratification at the salt screen.

Water levels were measured upstream and downstream of the salt screen with floater sensors with an accuracy of 0.1 mm. Additionally, the head difference over the salt screen was recorded for all measurements using a differential pressure cell with an accuracy of 0.03 mm. Vertical density profiles were measured at nine different locations in the model using vertical conductivity meters (VEZO's and GCM's, see Fig. 5). A VEZO gauge measures conductivity at 12 points in the vertical with an interval of 23 mm and a GCM gauge measures the conductivity at 8 points in the vertical at an interval of 67 mm. At each conductivity meter, temperature sensors were installed at the highest and lowest measurement points and these were used to derive the density profiles. Three conductivity gauges were movable (indicated with a "B" in Fig. 5), measuring the entire vertical salinity profile with an interval of 2 mm by continuously traversing the gauge up and down in the water column.

Three flow velocity components were measured in one location at the inlet and the horizontal flow velocity components were measured

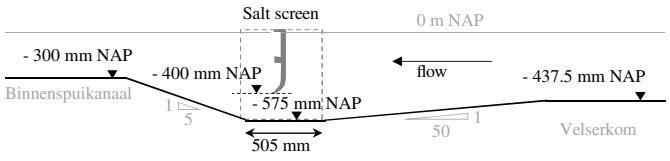

Fig. 4. Schematic representation of the floor levels along the axis of the salt screen; screen represented by solid shape and pillars by dashed rectangle.

Downloaded from ascelibrary.org by Technische Universiteit Delft on 01/09/23. Copyright ASCE. For personal use only; all rights reserved.

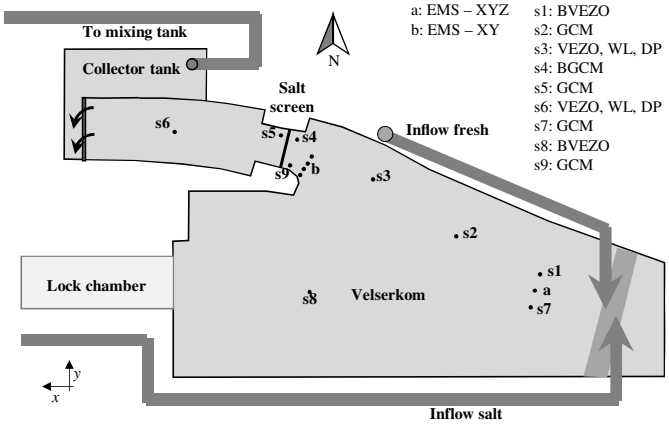

Fig. 5. Location of measurement instruments during testing (EMS: two velocity component measurements (at position a, two EMS devices are installed: one for the XY component and one for the XZ component), VEZO and GCM: vertical salinity profilers, WL: floaters, dP: differential pressure sensors).

at four locations upstream of the salt screen using two electromagnetic water velocity sensors (EMS) with a measuring frequency of 1 Hz. Detailed flow velocity measurements were also performed using three-dimensional particle tracking velocimetry (3D-PTV) and planar PIV (Adrian and Westerweel 2011). In addition, the general flow patterns were visualized and quantified by means of dye injection at various locations in the model.

Flow velocities were measured by means of PIV at five vertically oriented planes (P1 to P5–Fig. 6) distributed over the width of the salt screen. Two planes at $1/3$ breadth and $2/3$ breadth in the southern and northern opening and one plane in the middle of the center opening. For these measurements a double-pulsed laser (Nd:YAG, 532 nm green, Litron Lasers–Nano series) was used as a light source. Two monochrome CMOS cameras (Imager MX4M, LaVision, $2{,}048 \times 2{,}048$ pixels) imaged the field of view of approximately $0.6\ \text{m} \times 0.6\ \text{m}$ through the acrylic sidewalls near the salt screen. The objectives for cameras 1 and 2 had a 28 mm and 16 mm focal length, respectively. The image calibration was performed using a custom plate with a regular dot pattern. For the center plane (P3), the area between the two pillars could not be measured due to optical blockage by the pillar, resulting in a very limited field of view. Seeding particles with 100 μm diameter and particle density of 1,060 kg/m^3 (Vestosint®) were used to seed both the salt- and freshwater flow at the inlet such that the flow near the salt screen was not disturbed. The time between laser pulses was 26.3 ms, and the acquisition frequency of image pairs was 1 Hz. 600 images per

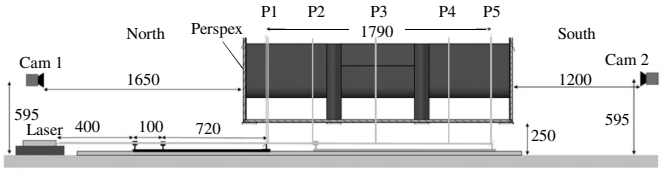

Fig. 6. Schematic sideview of the PIV setup with the measurement planes P1 to P5. The laser is positioned at the hall floor below the Perspex box with the salt screen. The laser beam is directed by means of lenses and mirrors to the correct measurement plane. Camera 1 captures the measurement planes P1 to P3 and Camera 2 captures the measurement planes P4 and P5. All dimensions are in mm.

measurement plane were recorded. The PIV cross-correlation was applied and the resulting vector spacing was 5.9 mm. The percentage of valid vectors was 95%–98%, except for the region downstream of the salt screen where mixing of the fresh and salt water occurred and in the mixing layer upstream of the salt screen, where a much lower valid vector percentage is found. Due to refraction of the laser light at the interface between salt and fresh water, the full vertical plane could not be measured with a single light source. For this reason, focus was given to properly capture the bottom salt layer.

After reaching a steady state condition, 3D-PTV measurements were carried out. For these tests, particles with a diameter of 20 mm and a known specific density were created with a 3D printer. Particles with a mass density of 1,020, 1,005, and 990 kg/m^3 followed the flow near the bottom, at the interface, and at the free surface, respectively. The particles were imaged simultaneously at 1 Hz by three color cameras with complementary metal–oxide–semiconductor (CMOS) sensors (Flir BlackFly 5.0 MP), which were mounted at approximately 9 m above the free surface of the model. The imaged region was approximately $8\ \text{m} \times 10\ \text{m}$ covering the upstream area of the salt screen. The extrinsic calibration was performed using ArUco markers at fixed positions on the model and the intrinsic calibration was performed separately using a checkerboard pattern and applying the algorithm as proposed by Heikkila and Silvén (1997). The particles were seeded to the flow at approximately 6 m upstream of the salt screen (see the three particle dispenser devices in Fig. 7), after which they attained their equilibrium depth and were transported by the flow toward the screen. This provided a uniform spreading of particles upstream of the screen as visible in Fig. 7. The surface particles were seeded manually over the upstream area, as the surface flow velocity was very small. The 3D-PTV algorithm was based on an extended version of the method as described in Duinmeijer et al. (2019).

The saltwater density was adjusted by mixing fresh water and brine (mainly NaCl with a brine density of approximately 1,200 kg/m^3), after which the conductivity was measured. The conductivity (σ) was converted into salinity (S) through the formula of Kohlraush and Holborn (1916), using the measurements of Labrique (1964) for the correction factor m_t for temperature (T) for a temperature range $0°\text{C} < T < 35°\text{C}$

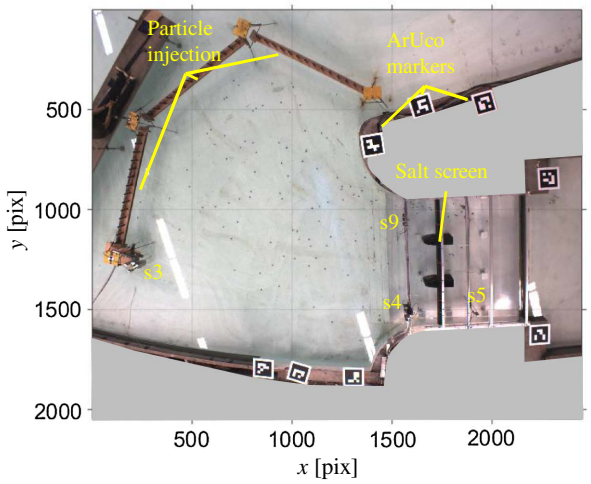

Fig. 7. Image of camera 1 used for 3D-PTV measurement. The tracer particles and the 8 ArUco markers are visible at the white floor of the scale model. The three particle dispensers are located in the upper left corner of the photo. The measurement stations s3–s5 and s9 are visible in the photo (see Fig. 5).

Downloaded from ascelibrary.org by Technische Universiteit Delft on 01/09/23. Copyright ASCE. For personal use only; all rights reserved.

$$S(T,\sigma) = \left(\frac{\sigma m_t}{2.134}\right)^{1/0.92} \quad (2)$$

with

$$m_t = \frac{1}{(0.008018T + 1.0609)^2 - 0.5911} \quad (3)$$

Using detailed measurement data, Delft Hydraulics Laboratory (1981) defined an equation for the conversion for salinity to density (ρ) for solutions prepared with NaCl with a maximum error of 26 ppm (2.5°C < T < 35°C; 0% < S < 35%), which is seen as a realistic compromise between the formula complexity and the correlated error:

$$\rho(T,S) = 999.904 + 4.8292 \cdot 10^{-2}T - 7.2312 \cdot 10^{-3}T^2 + 2.9963 \cdot 10^{-5}T^3 + 0.76427S - 3.1490 \cdot 10^{-3}TS + 3.1273 \cdot 10^{-5}T^2S \quad (4)$$

Various measurements were carried out covering different vertical density profiles and different levels of the interface. These tests were based on representative discharges in the Binnenspuikanaal, which range between 50 and 500 m^3/s with extreme discharges up to maximum 900 m^3/s. A discharge of 300 m^3/s (prototype value) was selected for the physical model tests, which is the expected turning point between fully and partially selective withdrawal. The tested conditions are listed in Table 1, covering tests with fresh water only and with varying ratios of fresh and salt discharges (Q_f/Q_s). To reach steady state conditions in the model, long spin up times were required. Test 300F ran for 38 hours over four measurement days. The three stops during the night had no significant impact on the density profiles as the profiles were recovered within one hour at the start of a new measurement day. Steady state conditions were judged by the rate of change of the vertical salinity profiles in all measurement points.

One test has been performed to investigate the transient behavior of the model. In this test (300G), the inflow discharge was stopped abruptly, after which internal waves were generated and recorded by the measurement devices.

Numerical Modeling

The validation of the numerical model (CFD) was carried out on the same domain and scale as the physical model. The boundary conditions were kept the same as much as possible. To assess the efficiency of the selective withdrawal in IJmuiden, additional CFD simulations at scale and in prototype dimensions were carried out using a velocity boundary at the outlet and a pressure boundary at the inlet. These simulations are not reported in this article as they were not part of the validation.

A CFD model of the physical scale model has been set up using the commercial software package StarCCM+, version 14.02.10 (STAR-CCM+ 2019). The mesh was generated using the built-in Star Trim mesher algorithm. The mesh has been generated in StarCCM+ using multiple areas of mesh refinement. The largest cells in the domain were located in the Velserkom and Binnenspuikanaal with a horizontal resolution of 10 cm and a vertical resolution of 2.5 cm. The slopes upstream and downstream of the salt screen contained cubic cells with a resolution of 2.5 cm and the area around the salt screen and the inner bend contained cubic cells with a resolution of 1.25 cm. The time step used in the unsteady RANS simulation was 0.015 s. The total number of cells for the simulations is approximately 7.3 million and the simulations took about four weeks to reach a steady solution using 40 cores on a cluster of an Intel Xeon E3-1276 v3 processors of 3.6 GHz.

De Loor et al. (2018) compared different turbulence models for buoyancy driven flows using StarCCM+ and found that the realizable k-ε model was able to correctly predict the mixing between shear layers in a stably stratified flow. This was attributed to the specific implementation of the buoyancy production terms in the turbulent kinetic energy and turbulent dissipation transport equations. As mentioned by Uittenbogaard (1989), the turbulent Reynolds number, $Re_t = \sqrt{k}L/\nu$ (with turbulent kinetic energy k, mixing length L, and kinematic viscosity ν) should be larger than 100, which is the critical value for artificial damping of the turbulent structures by viscous dissipation. This value was approximately 200 at the measured inflow velocity of the physical scale model, which is sufficiently high to simulate the mixing layer with high Reynolds turbulence models (Uittenbogaard 1989). Boschetti et al. (2017) simulated the hydraulic model tests of Delft Hydraulics (1973), which were validated by Jirka (1979) and found a good agreement between the numerical model and the 2D measurements for a similar model setup.

Due to the limited head difference over the model, a rigid lid approach was used for these simulations to reduce the computation time significantly compared to using a free water surface. The geometry of the CFD model was generated based on a 3D scan of the bathymetry of the physical scale model. The 3D scan was carried out using a Faro Focus 3D X130 laser scanner with a vertical accuracy of 1 mm. The spatial resolution of the scan is about 3 mm, which was converted into a bathymetry for the CFD model with a resolution of 2.5 cm. The velocity and density profile at the inlet of the CFD model was prescribed at 3 vertical sections, in the freshwater layer, in the mixing layer and in the saltwater layer. Using the continuity equation in combination with the densities and the measured flow velocity in the saltwater layer at the inlet (see measurement point "a" in Fig. 5), the corresponding flow velocities at the freshwater layer and in the mixing layer were derived. This resulted in a vertical density profile similar to the vertical density profile of

Table 1. Test program

Test ID	Type test	$z_{interface}$ (mm NAP)	Q_f/Q_s (l/s)	$\Delta\rho$ (kg/m^3)	PTV	PIV
300A	Determination discharge coefficient	N/A	29.6/0	0	—	—
900A	Determination discharge coefficient at max discharge	N/A	85.0/0	0	Y	—
300C	Density difference 1, sharp interface at high level	−300	1/28.6	15.9	Y	—
300D	Density difference 1, sharp interface at low level	−340	3/26.6	15.9	Y	—
300E	Density difference 2, sharp interface at low level	−340	3/26.6	7.4	Y	—
300F	Reference test, density difference 1, gradual interface	−340	7/22.6	15.9	Y	Y
100A	Lower discharge, density difference 1, gradual interface	−340	2.3/7.6	15.9	Y	—
Stop test (300G)	Transient test | reference test 300F | inflow stopped abruptly	−340	N/A	15.9	N/A	—

Note: Q_f = fresh discharge inflow; Q_s = salt discharge inflow; $\Delta\rho$ = density difference salt/fresh influx; and Y = measurement carried out.

Downloaded from ascelibrary.org by Technische Universiteit Delft on 01/09/23. Copyright ASCE. For personal use only; all rights reserved.

the measurements at the inlet. At the outlet, a Neumann boundary was present with a zero-gradient for pressure and velocity.

Results

The results of the scale model are presented for all tests and measurements that were carried out and the CFD model has been compared to test 300F with the most realistic condition.

Flow Behavior

At the inlet the salt and fresh water entered the scale model perpendicular to the inlet construction (Fig. 3). From the inlet, the water flowed over the downward sloping bed toward the salt screen. Due to the geometry of the southern bend and the local bathymetry, the flow tended to detach from the southern bend at the interface. Lower, in the salt layer, the flow generally remained attached to the southern bend and side wall. This led to a complex three-dimensional flow pattern at this location. In Figs. 8 and 9, the observed flow patterns upstream and around the salt screen are schematically shown. The indicators between brackets in the following section refer to the positions in Figs. 8 and 9. In the salt layer, the approach flow was generally perpendicular to the salt screen for all openings (1), while at the interface between fresh and salt water, the flow approached the screen at an angle (4), which led to a small recirculation zone at the interface (5). In the upper (fresh) part of the water column, the flow velocities upstream from the screen were very small and did not show a clear preference in direction. A large recirculation zone (6) was present at the interface level upstream of the screen attached to the northern bank of the approach area; a similar circulation pattern was also observed in the salt layer (2), in a smaller area close to the northern bank.

Due to little flow detachment in the salt layer, a return flow was present at the bed level at the southern side (3) immediately downstream of the screen. This return flow did not reach the screen. Downstream of the screen, a strong vertical upward flow was observed (7) at the north and central openings. This upwelling was caused by the relative fresh water that passes under the tip of the screen. At the southern opening, the flow patterns were different and the upward flow was less strong (8), as the salinity profile was less stratified. The flow velocities at the north side under the screen reached up to 12 cm/s, while the maximum was 7 cm/s at the south side for the discharge of 29.6 L/s.

The vertical flow velocities measured with PIV and simulated with the numerical model for planes P1 and P5 are shown in Fig. 10. The CFD model was able to capture the velocity patterns around the screen well. The upwelling behind the screen was well represented. The flow patterns around the screen depend on the approach flow conditions. More flow detachment at the southside will result in higher flow velocities at the northside of the screen. The CFD model predicted a slightly stronger flow detachment than what was observed in the physical model, which is shown in the flow velocity magnitudes below the screen. Because of continuity, this leads to a lower flow velocity in the southern opening in the CFD model (P5 of Fig. 10). Close to the southern wall, this even resulted in a return flow under the screen in the CFD model (not visible in P5 of Fig. 10), which was absent in the physical scale model.

Horizontal flow velocities were measured at the inflow of the physical scale model by means of two electromagnetic water velocity sensors at a distance of 10 cm above the bed. During a measurement period of 3 hours for test 300F (Table 1), an average

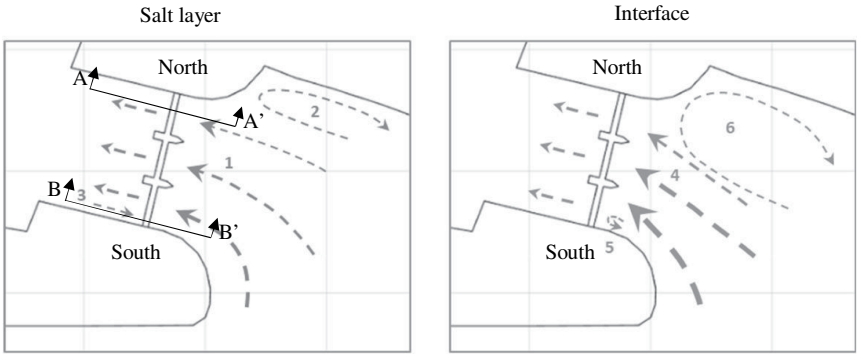

Fig. 8. Schematized flow patterns in the salt layer and at the interface, measured by means of PTV and dye injection.

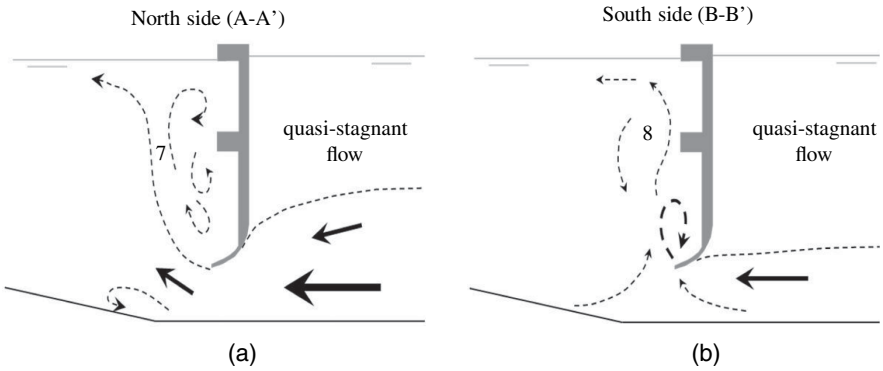

Fig. 9. Governing flow patterns around the screen at the (a) north side and (b) south side of the screen as measured by PIV and dye injection.

J. Hydraul. Eng., 2022, 148(2): 05021011

Downloaded from ascelibrary.org by Technische Universiteit Delft on 01/09/23. Copyright ASCE. For personal use only; all rights reserved.

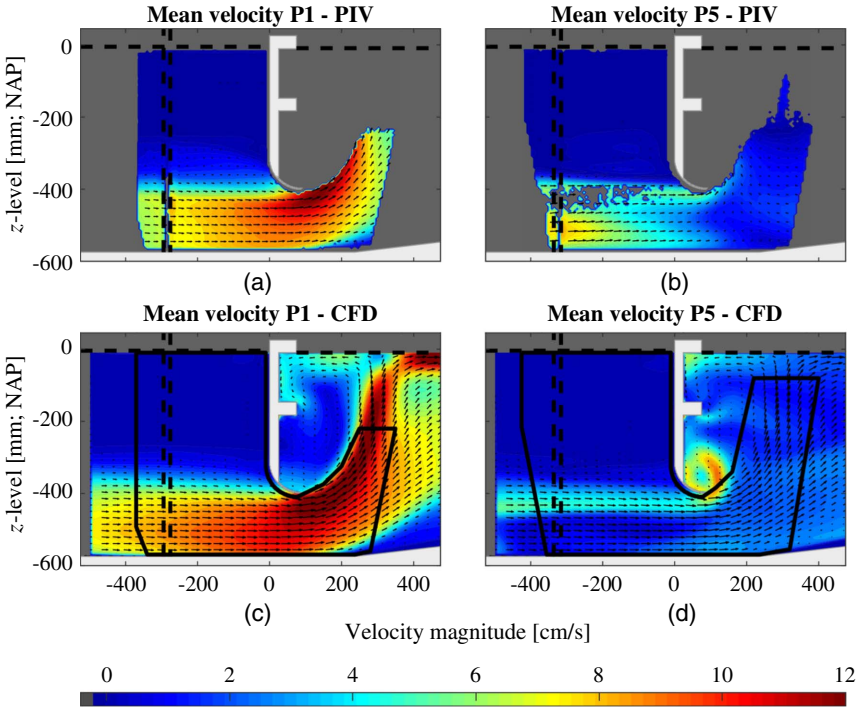

Fig. 10. Flow patterns for test 300F as measured by (a and b) PIV and (c and d) simulated for the plane at the northside of the screen (P1–a and c) and for the plane at the southside of the screen (P5–b and d). In the mixing zone, no measurements could be obtained with PIV. The dashed lines represent the water surface and the extend of the curved northern and southern sidewalls. The solid line (c and d) show the outline of the PIV measurements.

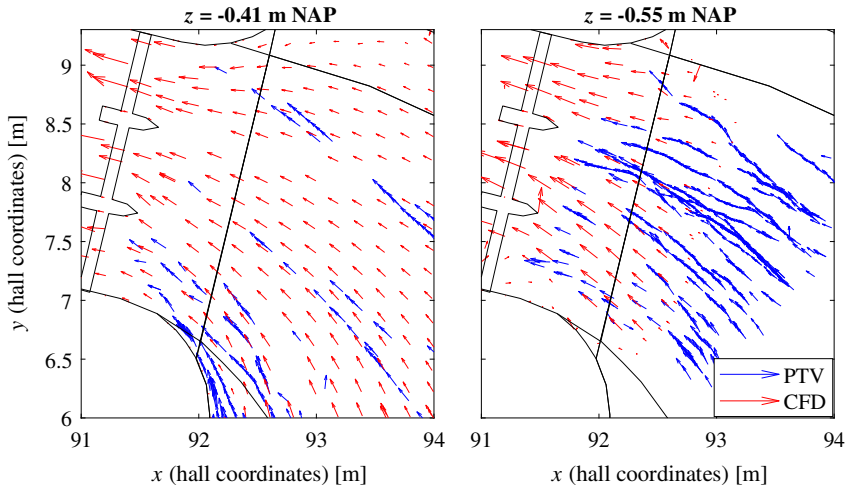

Fig. 11. Flow patterns for test 300F as measured by 3D-PTV and simulated for a horizontal plane immediately below the screen (−0.41 m NAP) and just above the bottom (−0.55 m NAP).

velocity of 8.14 cm/s was measured with a turbulent intensity (k) of 0.073 cm^2/s^2. Fig. 11 shows the flow patterns upstream of the salt screen derived from the 3D-PTV measurements and simulations at horizontal planes at the mixing layer immediately below the screen (−0.41 m NAP) and in the salt layer just above the bottom (−0.55 m NAP). The flow patterns at the mixing layer just below the screen are matching well at the south side. The measured flow patterns in the salt layer at the southern opening are slightly different. The measurements show a flow pattern toward the screen in front of the southern opening, while the simulations show a slightly more oblique flow. This indicates that the CFD model predicts a slightly larger zone of flow detachment. The arrows in the 3D-PTV measurements depict particle velocities.

Density Effects

The measured density profiles at various positions in the model (Fig. 5) are presented for all test conditions at the inlet and at the screen (Fig. 12), as well as for the case validated by the CFD model. In the model, a fixed inflow of salt and fresh water was defined for each test (Table 1). This also defined the withdrawal ratio ($\lambda = Q_{fresh}/Q_{total}$) as defined by Jirka (1979). This fixed inflow

Downloaded from ascelibrary.org by Technische Universiteit Delft on 01/09/23. Copyright ASCE. For personal use only; all rights reserved.

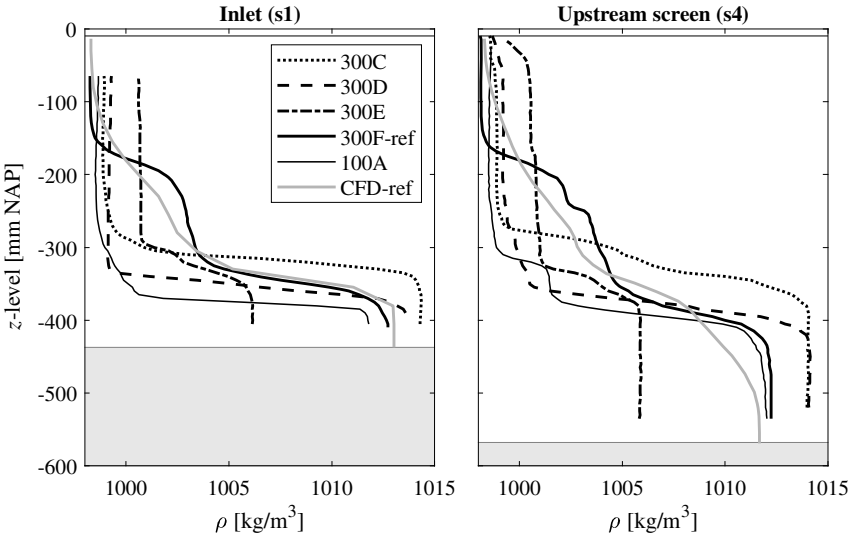

Fig. 12. Stationary vertical density profiles at the inlet (s1) and at the screen (s4) for each test condition. CFD-ref corresponds to test 300F-ref.

Table 2. Level interface of the interface at the inlet (s1) and upstream of the salt screen (s4) for different measurements (Fig. 5)

	Flow rate (l/s)			Level interface (mm; NAP)		Drop interface level (mm)	
Test	Fresh	Salt	Total	Inlet (s1)	Screen (s4)	Location s1–s4	Salt flux (kg/s)
100A	2.3	7.6	9.9	−374.3	−389.9	15.6	0.18
300C	1	28.6	29.6	−315.6	−323.3	7.7	0.67
300D	3	26.6	29.6	−356.0	−376.6	20.6	0.63
300F	7	22.6	29.6	−334.4	−358.1	23.7	0.54

condition resulted in a specific location of the interface between the two layers. The interface was evolving in the scale model from the inlet toward the outflow. The density change at the interface is rather strong in most tests. To obtain a profile which was more similar to the gradual profiles measured in prototype, the inflow for test 300F and 100A was modified by the installation of an additional vertical plate at the inlet section where the combined fresh and salt water needed to flow underneath. This resulted in additional mixing at the interface as shown in Fig. 12. Test 300E (reduced vertical density difference at inflow) was not successful in this respect. It did not quite reach a stable condition after 28 h since the freshwater zone was slowly mixing with salt water, resulting in gradually higher densities in the top layer and a weaker stratification.

The salt fluxes for these tests are given in Table 2 in relation to the level of the interface and the drop in the interface level between the inlet and the salt screen. The level of the interface in this table is defined as the level of mean density between the salt- and freshwater layers: $(\rho_{max} + \rho_{min})/2$. Although the salinity profiles differed between the tests, some basic conclusions could be drawn by comparing the level and the drop of the interface between the different tests. The strongly stratified profiles of tests 300C and 300D show that a higher salt flux through the model resulted in a higher level of the interface at the salt screen. Based on the comparison of test 100A and 300F with the same withdrawal rate, it was concluded that the level of the interface to the salt screen dropped more at higher discharges than at lower discharges, and it was observed that the level of the interface at the inlet is at a lower level for lower discharges than for higher total discharges. This means that it was not possible to keep an equal level of the interface at the inlet for low discharges without any changes to the withdrawal ratio. The drop of the interface level in test 300D was smaller than for test 300F (Table 2), while the level of the interface at the inlet was already lower in test 300D than in test 300F. This means that the drop in the interface level is correlated to the level of stratification of the profile. The findings listed previously provide some general insights on the relation between salt flux, the salinity profile, the development of the interface, and total discharge.

The development of the density profiles from the inlet to the outflow for test 300F is shown in Fig. 13 for both the measurement and the CFD simulation. The height of the interface in the measurements is slightly decreasing upstream of the salt screen, while a stronger decrease is observed in the CFD model. A three-dimensional effect is observed upstream of the salt screen, where the density profile at the southern bend (s9) in the measurements is more gradual than at the northern bend (s4).

In addition to the stationary conditions, a transient verification has been carried out (test 300G–Table 1) by abruptly stopping the inflow of the model. This resulted in internal waves both upstream and downstream of the salt screen. The internal wave velocity in the numerical model and the scale model test was compared, see Table 3. A stronger stratification leads to a higher internal wave velocity. Due to differences in stratification between the scale model and the numerical model, the internal waves travel slightly faster in the scale model than in the numerical model. The largest difference between the measured and the modeled internal wave velocity is found in the area upstream of the screen at the sloping bed. However, in general, the numerical model is able to represent the internal wave velocity accurately.

The effectiveness of selective withdrawal by the salt screen has been compared to the withdrawal rates based on Jirka (1979). The withdrawal ratio of the tests presented in this article with a complex three-dimensional nonuniform flow range from 0.03 for test 300C

Downloaded from ascelibrary.org by Technische Universiteit Delft on 01/09/23. Copyright ASCE. For personal use only; all rights reserved.

Downloaded from ascelibrary.org by Technische Universiteit Delft on 01/09/23. Copyright ASCE. For personal use only; all rights reserved.

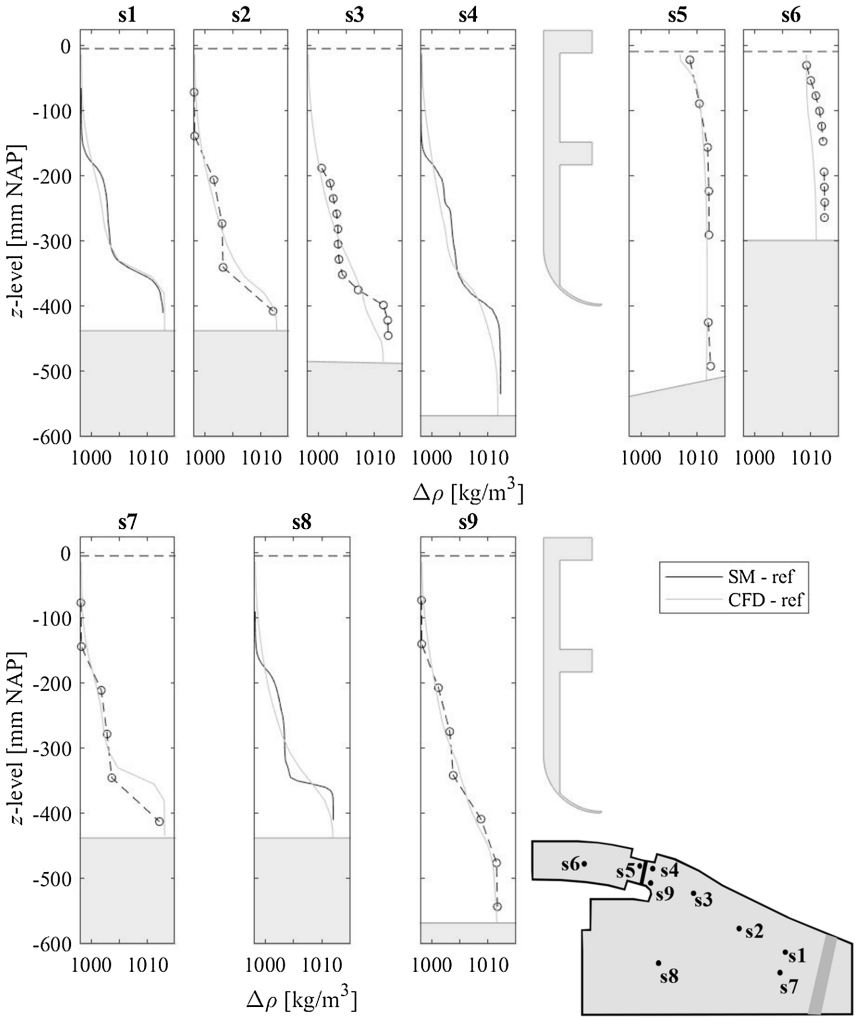

Fig. 13. Measured and modeled density profiles in the model. The dotted lines with markers indicate the fixed measurement points and the solid lines represent densities obtained from the moving conductivity gauges in test 300F.

Table 3. Measured and modeled internal wave velocity during stopping test

Location with respect to salt screen	Sensors	Distance (m)	Measured travel time (s)	Average depth (m; NAP)	Internal wave velocity	
					Scale model (cm/s)	CFD model (cm/s)
Upstream	s9-s3	4.85	42	0.528	11.5	8.3
	s3-s2	6.07	66	0.462	9.2	7.9
	s2-s7	6.13	63	0.438	9.7	8.1
Downstream	s5-s6	6.41	400	0.300	1.6	1.88

up to 0.24 for test 100A and 300F, while the withdrawal ratio for these tests would be zero based on the effectiveness diagrams of Jirka (1979). This means that Jirka (1979) would predict a fully effective selective withdrawal. This shows that the effectiveness diagrams of Jirka (1979) overestimate the effectiveness for complex three-dimensional geometries as present in the IJmuiden case.

Head Differences

For the freshwater tests 300A and 900A, the head difference is measured using the differential pressure sensor. Using the discharge formula $Q = \mu A\sqrt{2g\Delta h}$, where Q is the discharge, A is the cross-sectional area below the screen, g is the gravitational acceleration, and Δh is the head difference over the screen, a discharge coefficient (μ) of 0.83 is calculated. The discharge coefficients for the other measurements depend on the up- and downstream density profiles. Here, the head difference is derived from the floater sensors. The measured head differences of all tests are shown in Fig. 14.

For the test cases with a stronger stratification, the contribution of the density on the head difference is much larger than the flow velocity effects (in this case up to a factor of 8). This can lead to a situation where the head difference over the screen is smaller in periods with high discharges due to the supply of fresh water from the inland water system, compared to periods with low discharges when the stratification at the salt screen is stronger. The CFD model

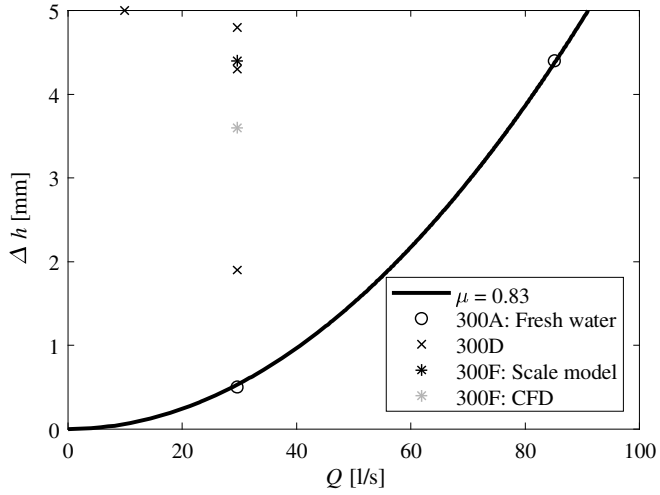

Fig. 14. Measured and modeled head differences at the salt screen for all test conditions. The solid line represents only freshwater tests (both tests gave a discharge coefficient of 0.83). The remaining dots depend on the density profiles as shown in Fig. 12.

computed a head difference of 3.6 mm compared to 4.4 mm in the scale model, see Fig. 14. An explanation for this difference could be related to the differences in measured and modeled density profiles at the location s3 and s6 (Fig. 13) and the derivation of the head on the pressure on the rigid lid in the CFD model.

Discussion

3D-PTV measurements have been used to study qualitatively the flow patterns upstream of the salt screen, in particular, the zone of flow detachment. For a more quantitative analysis, the drag force on the particles should be incorporated and the resistance of the bed on the heaviest particles should be studied. This has not been elaborated further.

The flow detachment at the southern bend upstream of the salt screen determined the effectiveness of the application. At the upstream boundary, a fixed inflow of salt and fresh water was prescribed. Because of this approach, differences in flow detachment at the southern bend resulted automatically in different flow velocities between the southern and northern side of the salt screen. Because the numerical model showed some more flow detachment at the southern side, stronger flow velocities appeared at the northern side of the salt screen, probably causing additional mixing.

Because the density plays a large role in the head differences over the salt screen, the discharge coefficient according to the earlier definition is variable in practice. At high discharges, with a larger supply of fresh water, the discharge coefficient may reach up to 0.83. This means that at high discharges, the head differences at the salt screen could eventually be lower than at low discharges with stratified conditions.

The effectiveness diagrams presented by Jirka (1979) could not be applied for this complex three-dimensional flow situation, as this diagram predicted a fully effective withdrawal for the tested conditions. It would match better if a correction was made for the effective cross-sectional area under the salt screen after detachment of the flow at the southern bend. For the tested cases, the withdrawal ratio presented by Jirka (1979) changes rapidly for higher Froude numbers, which causes uncertainty in the prediction of the withdrawal ratio. Additionally, the withdrawal ratio by Jirka (1979) are based on sharp interfaces between salt and fresh water. As gradual interfaces are normally present in prototype conditions near IJmuiden, the effectiveness of selective withdrawal in these situations should be investigated differently.

In order to verify that the investigated salt screen design effectively mitigates the effects of the extra salt inflow by the new lock, longer timespans should be studied considering varying discharges and lock operations. This can only be carried out by large scale models in prototype covering the hydrodynamic system including the full Binnenspuikanaal and upstream canal system.

Conclusion

Selective withdrawal can be used as an effective measure to mitigate this salt intrusion. The concept of selective withdrawal has been studied by various researchers in the past, where design formulas are presented by Jirka (1979) to assess the effectiveness of a skimmer wall for selective withdrawal. However, as nonuniform three-dimensional effects may influence the effectiveness of a skimmer wall, the use of these formulas, which were based on two-dimensional applications, may lead to significant discrepancies between predicted and achieved withdrawal ratios. For the case of the proposed salt screen at IJmuiden presented in this article, the design formulas by Jirka (1979) would predict a full selective withdrawal, whereas partial selective withdrawal, up to $\lambda = 0.24$, was found in the physical model. For this reason, these nonuniform three-dimensional effects were studied in detail during the design phase of a salt screen.

For the new salt screen at IJmuiden, nonuniform three-dimensional effects of partial selective withdrawal have been studied by means of both physical and numerical scale modeling. A physical scale model was built at scale 1:40 to study the performance of selective withdrawal and the 3D flow patterns around the salt screen at IJmuiden. Spatially distributed density measurements and detailed flow velocity measurements using PIV and 3D PTV around the salt screen were performed to get a detailed insight into the complex 3D flow behavior near the salt screen. Internal wave behavior has been studied by means of an abrupt stop of the flows in the model.

A 3D numerical model has been validated against the flow patterns, density profiles, and internal wave behavior of the physical scale model experiments. The detailed flow patterns including turbulent mixing, buoyancy effects, oblique flows, and flow detachment were compared. Although the numerical model produced somewhat more mixing over the vertical and a slightly stronger flow detachment at the southern side wall than the physical model, the characteristic flow patterns were adequately reproduced by a RANS model with a rigid lid surface and using the realizable k-ε turbulence model. The validation of the CFD model against the physical scale measurements has shown that detailed numerical modeling can be used to design salt screens in areas where simpler design formulas do not apply and to study the impact of nonuniform three-dimensional flow patterns on the effectiveness of such salt screens.

Data Availability Statement

Some or all data, models, or code generated or used during the study are available in a repository online in accordance with funder data retention policies. The measurement data set can be obtained through the Deltares Data Portal (https://deltaresdata.openearth.eu/).

Downloaded from ascelibrary.org by Technische Universiteit Delft on 01/09/23. Copyright ASCE. For personal use only; all rights reserved.

Acknowledgments

Rijkswaterstaat is acknowledged for their permission to publish this study and to make the measurement data and simulation results available. The authors are grateful to Wim Uijttewaal and Robert Jan Labeur of the TU Delft for the stimulating discussions during the execution of both the physical and numerical model tests.

References

Abraham, G., and P. van der Burgh. 1964. "Pneumatic reduction of salt intrusion through locks." *J. Hydraul. Div.* 90 (1): 83–119. https://doi.org/10.1061/JYCEAJ.0001009.

Adrian, R. J., and J. Westerweel. 2011. *Particle image velocimetry*. New York: Cambridge University Press.

Boschetti, T., T. O'Mahoney, and A. C. Bijlsma. 2017. *CFD modelling of the mitigation of salt intrusion by selective withdrawal*. Eindhoven, Netherlands: Eindhoven Univ. Technology.

Delft Hydraulics Laboratory. 1958. *Scaling rules for research on density currents*. [In Dutch.] Report Id: R0937. Delft, Netherlands: Delft Hydraulics Laboratory.

Delft Hydraulics Laboratory. 1973. *Discharge sluice Noordland in the Eastern Scheldt dam, Selective withdrawal, two-dimensional investigation*. [In Dutch.] Report Id: M1204. Delft, Netherlands: Delft Hydraulics Laboratory.

Delft Hydraulics Laboratory. 1981. *New accurate density formulations for pure water and saline solution: Density as a function of temperature and salt concentrations*. [In Dutch.] Report Id: S205-1. Delft, Netherlands: Delft Hydraulics Laboratory.

De Loor, A., R. E. Uittenbogaard, and A. C. Bijlsma. 2018. "Evaluation of RANS turbulence models for buoyancy driven flows using Star-CCM+." In *Proc., 5th IAHR Europe Congress Trento*, 213–214. Paris: International Association for Hydro-Environment. https://doi.org/10.3850/978-981-11-2731-1_124-cd.

Duinmeijer, S. P., A. M. Moreno-Rodenas, M. Lepot, C. van Nieuwenhuizen, I. Meyer, and F. H. Clemens. 2019. "A simple measuring set-up for the experimental determination of the dynamics of a large particle in the 3D velocity field around a free surface vortex." *Flow Meas. Instrum.* 65 (Mar): 52–64. https://doi.org/10.1016/j.flowmeasinst.2018.10.007.

Ettema R., M. Muste, J. Odgaard, P. Ryan, F. Locher, and S. Tu. 2005. "A continuously operable hydraulic model of selective withdrawal from a stratified reservoir." In *Proc., 31st IAHR World Congress*, 1751–1758.

Fan, J. 2008. "Stratified flow through outlets." *J. Hydro-environ. Res.* 2 (1): 3–18. https://doi.org/10.1016/j.jher.2008.04.001.

Farrow, D. E., and G. C. Hocking. 2006. "A numerical model for withdrawal from a two-layered fluid." *J. Fluid Mech.* 549: 141–157. https://doi.org/10.1017/S0022112005007561.

Harleman, D. R. F., and R. A. Elder. 1965. "Withdrawal from two-layer stratified flows." *J. Hydraul. Div.* 91 (4): 43–58. https://doi.org/10.1061/JYCEAJ.0001294.

Heikkila, J., and O. Silvén. 1997. "A four-step camera calibration procedure with implicit image correction." In *Proc., 1997 IEEE Computer Society Conf. on Computer Vision and Pattern Recognition*, 1106–1112. New York: IEEE.

Hocking, G. C. 1991. "Withdrawal from two-layer fluid through line sink." *J. Hydraul. Eng.* 117 (6): 800–805. https://doi.org/10.1061/(ASCE)0733-9429(1991)117:6(800).

Hocking, G. C. 1995. "Supercritical withdrawal from a two-layer fluid through a line sink." *J. Fluid Mech.* 297: 37–47. https://doi.org/10.1017/S0022112095002990.

Imberger, J. 1980. *Selective Withdrawal: A review*. Trondheim, Norway: Norwegian Institute of Technology Trondheim Norway.

Islam, M. R., I. Wood, and D. Z. Zhu. 2018. "Selective withdrawal from an intake channel connected to a reservoir." *J. Eng. Math.* 111 (1): 79–94. https://doi.org/10.1007/s10665-018-9955-9.

Jirka, G. H. 1979. "Supercritical withdrawal from two-layered fluid systems." *J. Hydraul. Res.* 17 (1): 43–51. https://doi.org/10.1080/00221687909499599.

Jirka, G. H., and D. S. Katavola. 1979. "Supercritical withdrawal from two-layered fluid systems part 2: Three-dimensional flow into round intake." *J. Hydraul. Res.* 17 (1): 53–62. https://doi.org/10.1080/00221687909499600.

Kerstma, J., P. A. Kolkman, H. J. Regeling, and W. A. Venis. 1994. *Water quality control at ship locks: Prevention of salt- and fresh water exchange*. Rotterdam, Netherlands: A.A. Balkema.

Kohlraush, F., and L. Holborn. 1916. *Das Leitvermögen der Electrolyte—Insbesondere der wasserigen losungen*. Leipzig und Berlin: B.G. Teubner.

Labrique, J. P. 1964. "Portable conductivity meters for low or medium salinity measurements." *J. Hydrol. Sci.* 9 (4): 58–62. https://doi.org/10.1080/02626666409493688.

Mausshardt, S., and G. Singelton. 1995. "Mitigating salt-water intrusion though Hiram M. Chittenden locks." *J. Waterw. Port Coastal Ocean Eng.* 121 (4): 224–227. https://doi.org/10.1061/(ASCE)0733-950X(1995)121:4(224).

Monish, B. M. 1938. "Discussion of the passage of turbid water through Lake Mead." *Transactions* 103 (1): 751–755. https://doi.org/10.1061/TACEAT.0004929.

Nogueira, H. I., P. van der Ven, T. O'Mahoney, A. De Loor, A. van der Hout, and W. Kortlever. 2018. "Effect of density differences on the forces acting on a moored vessel while operating navigation locks." *J. Hydraul. Eng.* 144 (6): 04018021. https://doi.org/10.1061/(ASCE)HY.1943-7900.0001445.

Shamaa, Y., and D. Z. Zhu. 2010. "Experimental study on selective withdrawal in a two layer reservoir using a temperature-control curtain." *J. Hydraul. Eng.* 136 (4): 234–246. https://doi.org/10.1061/(ASCE)HY.1943-7900.0000165.

STAR-CCM+. 2019. "Simcenter STAR-CCM+." Accessed December 5, 2019. https://www.plm.automation.siemens.com/global/en/products/simcenter/STAR-CCM.html.

Thendrup, A. 1980. "Selective withdrawal with multiple constrictions and non-linear density profiles." In *Proc., 2nd Symp. on Stratified Flows*, 381–400. Trondheim, Norway: Norwegian Institute of Technology Trondheim Norway.

Uittenbogaard, R. E. 1989. "Measurement of turbulent fluxes in a steady, stratified, mixing layer." In *Proc., 3rd Int. Symp. Refined Flow Modelling and Turbulence Measurements*, 863–871. Tokyo: Universal Academy Press.

Van den Brink, M., Y. Huismans, M. Blaas, and G. Zwolsman. 2019. "Climate change induced salinization of drinking water inlets along a tidal branch of the Rhine river: Impact assessment and an adaptive strategy for water resources management." *J. Clim.* 7 (4): 49. https://doi.org/10.3390/cli7040049.

Van der Kuur, P. 1986. "Locks with devices to reduce salt intrusion." *J. Waterw. Port Coastal Ocean Eng.* 111 (6): 1009–1021. https://doi.org/10.1061/(ASCE)0733-950X(1985)111:6(1009).

Wood, I. R. 2001. "Extensions to the theory of selective withdrawal." *J. Fluid Mech.* 448: 315–333. https://doi.org/10.1017/S002211200100605X.

Wood, I. R., and K. K. Lai. 1972. "Selective withdrawal from two-layer fluid." *J. Hydraul. Res.* 10 (4): 475–496. https://doi.org/10.1080/00221687209500036.

Yu, W. S., S. M. Hsu, and K. L. Fan. 2004. "Experiments on selective withdrawal of a codirectional two-layer flow through a line sink." *J. Hydraul. Eng.* 130 (12): 1156–1166. https://doi.org/10.1061/(ASCE)0733-9429(2004)130:12(1156).

Downloaded from ascelibrary.org by Technische Universiteit Delft on 01/09/23. Copyright ASCE. For personal use only; all rights reserved.